 https://doi.org/10.3311/PPch.36825

Periodica Polytechnica Chemical Engineering, 68(3), pp. 348–363, 2024

Study and Optimization of a New Perovskite Solar Cell Structure Based on the Two Absorber Materials Cs_2TiBr_6 and $MASnBr_3$ Using SCAPS 1D

Keltoum Dris[1,2], Mostefa Benhaliliba[1*]

[1] Film Device Fabrication-Characterization and Application (FDFCA) Research Group, University of Science and Technology Mohamed Boudiaf (USTOMB), 31130 El M'naouer, Oran, P.O.B. 1505, Algeria
[2] Laboratoire D'études Physiques des Matériaux, University of Science and Technology Mohamed Boudiaf (USTOMB), 31000 El M'naouer, Oran, P.O.B. 1505, Algeria
[*] Corresponding author, e-mail: mostefa.benhaliliba@univ-usto.dz

Received: 08 March 2024, Accepted: 26 June 2024, Published online: 24 July 2024

Abstract

The main objective of this study is to optimize the photovoltaic parameters of a new perovskite solar cell structure (PSC) suggested, using the simulator solar cell capacitance simulator-one dimension (SCAPS-1D) which aims to improve its performance by adjusting different key variables. This new suggested cell which consists of six materials represents the major innovation point of our research, it is distinguished by a double active layer, composed of the two-cesium titanium hexabromide (Cs_2TiBr_6) and methylammonium tin tribromide ($MASnBr_3$) perovskites. Using the SCAPS 1D software, the simulation allows to determine the optimal values of the various parameters to maximize the efficiency of the PSC. First, the effect of the thickness and defect densities of both Cs_2TiBr_6 and $MASnBr_3$ materials on the output parameters was studied as well as the defect density in the interfaces. Subsequently, the doping density in Cs_2TiBr_6 and $MASnBr_3$ was also optimized. Finally, the impact of temperature, series resistance and shunt resistance were evidenced. The results indicate that precise adjustments of these parameters can lead to significant improvements in photovoltaic performance, such as open circuit voltage of 1.105 V, short-circuit current density of 33.90 mA cm^{-2}, fill factor of 88.01% and power conversion efficiency (PCE) 32.96%. These performances were obtained for a thickness of 700 nm for Cs_2TiBr_6 and 900 nm for $MASnBr_3$, a defect density of 10^{14} cm^{-3} for each absorber layer, a defect density of 10^{14} cm^{-2} for each interface and a doping density of the order of 10^{18} cm^{-3} for each absorbent layer.

Keywords

perovskite solar cell, power conversion efficiency, $MASnBr_3$, Cs_2TiBr_6, optimization

1 Introduction

Due to its low cost and easy manufacturing process, perovskite is a third-generation solar cell, which has the potential to become the dominant photovoltaic technology in the modern world [1]. The effectiveness of typical organic-inorganic hybrid perovskite solar cells (PSCs) such as formamidinium lead halide ($FAPbX_3$) and methylammonium lead halide ($MAPbX_3$), was improved from 3.8% in 2009 to more than 26% in 2021 [1–3].

Despite their exceptional optoelectronic qualities, lead-based organic-inorganic hybrid PSCs have significant disadvantages such as reduced shelf life, instability due to organic cations, lead-based absorber, which is dangerous to the environment. Therefore, the researchers proposed to find a more effective alternative to the hybrid inorganic-organic lead-based absorber. This leads to the introduction of all lead-free organic-inorganic perovskite and inorganic PSCs.

Alternatively, the toxic lead ion in methylammonium (MA) lead triiodide ($MAPbI_3$) is substituted with tin and germanium. Pewter-based perovskite structures are considered advantageous as absorbers for high-yield PSCs. Recently, several researchers have reported new perovskite-based PSCs without the need for lead [4–6].

Using numerical modelling Islam et al. studied the impact of amphoteric and interface defects on the $J - V$ (current density – voltage) characteristics of methylammonium tin tribromide ($MASnBr_3$)-based PSC, this cell achieved an efficiency of 21.66% [7]. The tolerance

Cite this article as: Dris, K., Benhaliliba, M. "Study and Optimization of a New Perovskite Solar Cell Structure Based on the Two Absorber Materials Cs_2TiBr_6 and $MASnBr_3$ Using SCAPS 1D", Periodica Polytechnica Chemical Engineering, 68(3), pp. 348–363, 2024. https://doi.org/10.3311/PPch.36825

factor Goldschmidt played an important role in the development of perovskites. By adjusting the perovskites composition, it is now employed to create and construct new stable organic-inorganic perovskite structures. To achieve the stable perovskite range, the tolerance factor can be adjusted by combining different X anions and A/B cations in a certain composition [8]. Therefore, it can be said that the suggested perovskite structure ($MASnBr_3$) is an excellent alternative to the most effective and stable lead-free PSC [9].

On the other hand, titanium is abundant on earth, thermally stable, biocompatible and non-toxic [10]. Chen et al. reported an FTO/TiO_2/Cs_2TiBr_6/P3HT/Au structure with a stable power conversion efficiency (PCE) up to 2.15% and an FTO/TiO_2/C_{60}/Cs_2TiBr_6/P3HT/Au structure with a stable PCE up to 3.22%. They used inorganic cesium titanium hexabromide (Cs_2TiBr_6) as perovskite and used inorganic titanium dioxide (TiO_2) and organic poly(3-hexylthiophene) (P3HT), buckminsterfullerene (C_{60}) charging materials [11].

Islam and Paul proposed and optimized a new heterojunction PSC structure based on three perovskite materials according to the configuration (FTO/ZnO/Cs_2TiCl_6(n)/Cs_2TiI_6(i)/Cs_2TiBr_6(p)/NiO/Pt), this optimized structure produced a PCE of 27.36% [12].

Using SCAPS 1D a comparative study was carried out by Ashfaq et al., in which several models of PSC based on absorbing material cesium titanium halide Cs_2TiX_6 ($X = Br^-, Cl^-, I^-$), a cell based on two perovskite materials of these models, and which has the configuration FTO/IZGO/Cs_2TiBr_6/Cs_2TiCl_6/$CuSbS_2$/Se produced an efficiency of about 30.06% [13]. Many analytical methods had been used to improve the performance of solar cells. For example, in a recent study, and using solar cell capacitance simulator-one dimension (SCAPS 1D) software, Mortadi et al. optimized PSCs, studying the effect of the band gap energy variation from 1.55 to 1.67 eV based on impedance spectroscopy. The results indicated that the cell achieves the best efficiency for a gap of 1.61 eV [14]. Mortadi et al., conducted another study based on impedance spectroscopy using the SCAPS 1D simulator to optimize PSC performance. They examined the effect of the perovskite layer thickness. The results demonstrated that the cell reached maximum efficiency when for an optimal thickness of 700 nm [15].

Since fabricating the different layers of a multilayer PSC is expensive and time-consuming, simulation studies and modeling are needed to determine acceptable materials for the different PSC layers. In this work, a new model of PSC had been proposed and optimized based on two perovskite materials one is inorganic and the other is organic-inorganic. This cell had the configuration (Au/MoO_3/Cs_2TiBr_6/$MASnBr_3$/ZnO/FTO) as drawn in Fig. 1 displaying its energy diagram. Cesium titanium bromide (Cs_2TiBr_6) was chosen as the first absorber of the cell due to its excellent absorption properties [16]. It had a long diffusion length of charge carriers, efficient photoluminescence and energy levels suitable for use in tandem solar cells. In addition, it also had superior thermal stability, light stability and moisture stability superior to

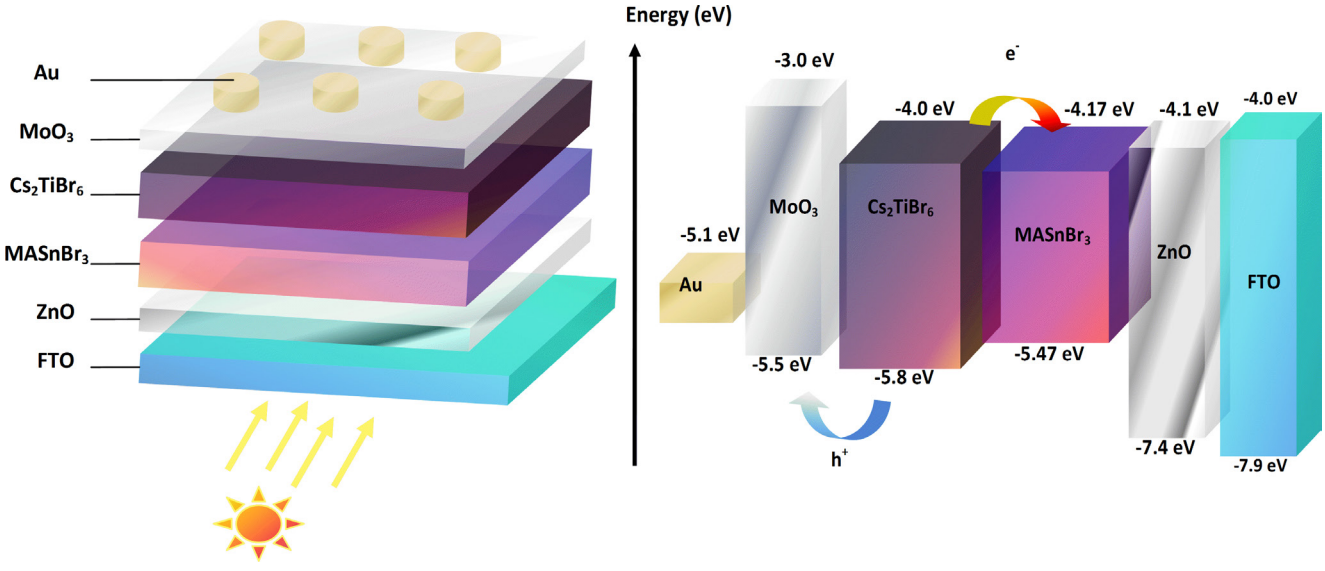

(a) (b)

Fig. 1 (a) The structure of (Au/MoO_3/Cs_2TiBr_6/$MASnBr_3$/ZnO/FTO), and (b) its energy band diagram

methylammonium lead iodide film ($MAPbI_3$), ensuring that Cs_2TiBr_6 film had intrinsic stability or higher environmental stability. In addition, Cs_2TiBr_6-based PSCs experimentally achieved an efficiency of 3.3%, which is higher than most other dual PSCs [17].

Methyl ammonium tin bromide ($CH_3NH_3SnBr_3$ or $MASnBr_3$) was used as the second absorber of the cell due to its good optical properties, good optical conductivity, narrow band deviation about 1.3 eV and good carrier mobility [6, 18]. ZnO was selected as electron transport material (ETM) [19, 20], and molybdenum trioxide (MoO_3) as hole transport material (HTM) [21]. Gold with a working function of 5.1 eV was taken as the front contact [22], while fluorine-doped tin oxide (FTO) was taken as the rear contact [23].

2 Computational method

In recent years, thin-film cell simulation had become more and more widely used, which is the reason why the research community in this field developed a variety of computers and simulation software. Solar cell capacitance simulator-one dimension (SCAPS 1D) is a software for numerical simulation of heterojunction thin film solar cells. It was developed by Burgelman et al. at Ghent University, Belgium, using Lab Windows/CVI from National Instruments [24]. After the 2nd Photovoltaic (PV) of the World Conference in 1998, it was opened to research universities in the photovoltaic community [24]. The SCAPS 1D program solved structural equations containing a series of semiconductor layers with arbitrary doping profiles (as a function of position) and arbitrary donor energy distributions or acceptor deep levels under several illumination types. Iterations of solving equations were made up to the algorithm convergence. SCAPS 1D was introduced in the literature with the articles. While the SCAPS algorithms detailed in the SCAPS references were originally developed for $CuInSe_2$ and CdTe family cell structures. However, several extensions improved its capabilities to become applicable for crystalline (Si and GaAs) solar cells, as well as amorphous (a-Si and Si micromorphs) solar cells [22, 25–27].

The software can simulate a solar cell consisting of seven layers, each with different properties such as doping profile, thickness, energy distribution at the donor or acceptor level, light absorption. It calculates the concentration, energy bands and current as well as $J-V$ properties. The surrogate properties and spectral response are determined by solving three main equations (Eqs. (1) to (3)):

- The Poisson equation [4]:

$$-\frac{\partial}{\partial x}\left[-\varepsilon(x)\frac{\partial V}{\partial x}\right]=q\begin{bmatrix}p(x)-n(x)\\+N_D^+(x)-N_A^-(x)\\+p_t(x)-n_t(x)\end{bmatrix}. \tag{1}$$

- The hole continuity equation [4]:

$$\frac{\partial P}{\partial t}=\frac{1}{q}\frac{\partial J_P}{\partial x}+G_P-R_P. \tag{2}$$

- The electron continuity equation [4]:

$$\frac{\partial n}{\partial t}=\frac{1}{q}\frac{\partial J_n}{\partial x}+G_n-R_n. \tag{3}$$

For the current density of holes and electrons, the equations are [12]:

$$J_P=qp\mu_p E+D_p\frac{dp}{dx}, \tag{4}$$

$$J_n=qp\mu_n E+D_n\frac{dn}{dx}. \tag{5}$$

In the steady-state condition, where: $\partial n/\partial t=0$, the electron continuity equation becomes [12]:

$$\frac{1}{q}\frac{\partial J_n}{\partial x}=-G_n(x,t)+R_n(x,t). \tag{6}$$

By substituting J_P from its previous expression, it follows [12]:

$$\frac{dE}{dx}+\mu_n\frac{dn}{dx}+D_n\frac{\partial^2 n}{\partial x^2}=-G_n(x)+R_n(x). \tag{7}$$

Similarly, for holes [12]:

$$\frac{dE}{dx}+\mu_p\frac{dp}{dx}+D_p\frac{\partial^2 p}{\partial x^2}=-G_p(x)+R_p(x). \tag{8}$$

SCAPS-1D can easily adapt many physical input parameters, facilitating complex calculations to evaluate device performance under various conditions [12].

With [4, 12]: q is the charge, V is the potential, ε is dielectric permeability, $n(x)$ is concentration of free electrons, $p(x)$ is concentration of free holes, $N_A^-(x)$ is the concentration of the ionized acceptor, $N_D^+(x)$ is the ionized donor concentration, G_P is the hole generation rate, G_n is the rate of generation of electrons, $n_t(x)$ is the electron trap density, $p_t(x)$ is the hole trap density, R_P is the recombinant rate of the hole, R_n is the rate of recombination of an electron, J_P is the current density of the hole, J_n is the current

density of the electron, μ_n is the mobility of electrons, μ_p is the mobility of holes.

To optimize the above cells, the effect of various parameters such as thickness, doping density and defect density of each absorbent layer as well as interface defect density, temperature, series resistance (R_s) and shunt resistance (R_{sh}) were studied. Simulations were performed using SCAPS-1D software version 3.3.07, using the input parameters listed in Tables 1 and 2, under standard test conditions: Air Mass 1.5 Global (AM1.5G) solar spectrum, temperature 300 K and power density 1000 W m^{-2} [28].

3 Results and discussion

3.1 Optimization of Cs_2TiBr_6 and $MASnBr_3$ layers thickness

The development of solar cells in particular PSC requires optimizing the thickness of the active layer (perovskite). The active or absorbent layer is the layer that absorbs the energy of photons and converts it into electrical energy. The photons number absorbed is directly affected by this layer thickness which affects the function of the cell.

Therefore, the first step towards improving the performance of the proposed Au/MoO_3/Cs_2TiBr_6/$MASnBr_3$/ZnO/FTO cell in this work is to optimize the two active layer Cs_2TiBr_6 and $MASnBr_3$ thicknesses. First, the thickness of the Cs_2TiBr_6 layer was varied from 100 to 1300 nm while all other parameters for the different layers of the cell – listed in Tables 1 and 2 – were fixed. Once the optimal thickness of Cs_2TiBr_6 was determined, it was set to its optimal value to optimize the perovskite second layer thickness $MASnBr_3$ which was varied between 100 and 1300 nm.

For the first Cs_2TiBr_6 layer, the effect of Cs_2TiBr_6 thickness variation on photovoltaic parameters and $J-V$ characteristics are sketched in Fig. 2. From these graphs it was found that the increase in the Cs_2TiBr_6 layer thickness decreased the fill factor (FF) slightly from 88.729% for 100 nm to 88.725% for 1300 nm, contrary to the results of Ashfaq et al., which observed a slight increase in FF [13]. The short-circuit current density (J_{sc}) showed a slight increase from 32.29 to 32.34 mA cm^{-2} for the thicknesses from 100 to 700 nm of the Cs_2TiBr_6 layer, and beyond 700 nm, the J_{sc} saturates. Similarly, the open

Table 1 Parameters of the used materials (MoO_3, Cs_2TiBr_6, $MASnBr_3$, ZnO, FTO) in cell simulation

Parameters	MoO_3 (HTM)	Cs_2TiBr_6	$MASnBr_3$	ZnO (ETM)	FTO
Thickness (nm)	100	100	500	100	100
Band gap (eV)	3.0	1.8	1.3	3.3	3.5
Electron affinity (eV)	2.5	4.0	4.17	4.1	4.0
Dielectric permittivity	12.5	10.0	10.0	9.0	9.0
CB effective density of states ($\times 10^{18}$ cm^{-3})	2.2	60	2.2	4	2.2
VB effective density of states ($\times 10^{18}$ cm^{-3})	1.8	21.4	1.8	10	18
Electron thermal velocity ($\times 10^7$ cm s^{-1})	1.0	1.0	1.0	1.0	1.0
Hole thermal velocity (cm s^{-1})	1.0×10^7	1.0×10^7	1.0×10^7	1.0×10^7	1.0×10^7
Electron mobility (cm^2 V^{-1} s^{-1})	25	0.23	1.6	100	20
Hole mobility (cm^2 V^{-1} s^{-1})	100	0.17	1.6	25	10
Shallow uniform donor density N_D (cm^{-3})	0	0	0	1.0×10^{20}	2×10^{19}
Shallow uniform acceptor density N_A ($\times 10^{18}$ cm^{-3})	1.0	3.0	10	0	0
N_t ($\times 10^{14}$ cm^{-3}) total	10	41.7	1.0	10	100
Reference	[21]	[16]	[4]	[20]	[23]

Table 2 The input parameters for the HTM/Cs_2TiBr_6, Cs_2TiBr_6/$MASnBr_3$ and $MASnBr_3$/ETM interfaces

Interface layer	MoO_3/Cs_2TiBr_6	Cs_2TiBr_6/$MASnBr_3$	$MASnBr_3$/ZnO
Type of defect	Neutral	Neutral	Neutral
Electrons capture cross-section (cm^2)	1.0×10^{-19}	1.0×10^{-19}	1.0×10^{-19}
Hole capture cross-section (cm^2)	1.0×10^{-19}	1.0×10^{-19}	1.0×10^{-19}
Energy distribution	Single	Single	Single
Defect energy level reference (E_t)	Above the highest energy valence (EV)	Above the highest EV	Above the highest EV
Energy level related to reference (eV)	0.6	0.6	0.6
Total density integrated over all energies (cm^{-3})	1.0×10^{10}	1.0×10^{10}	1.0×10^{10}

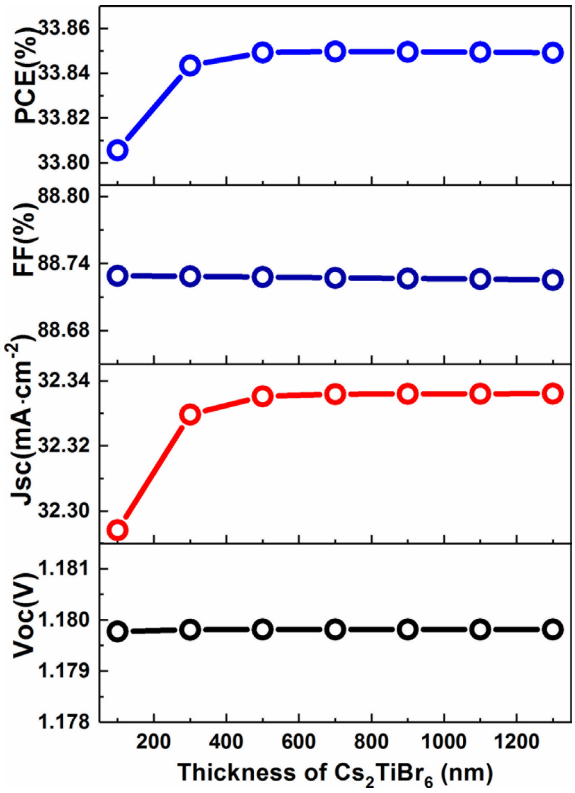

(a)

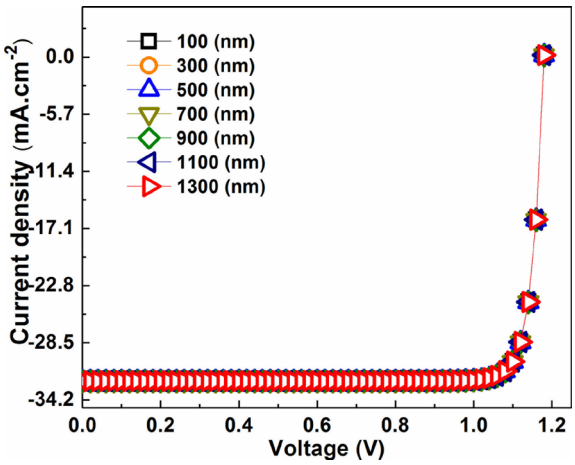

(b)

Fig. 2 (a) The effect of Cs_2TiBr_6 layer thickness on photovoltaic parameters of PSC device and on (b) $J - V$ characteristics

circuit voltage (V_{oc}) showed a slight improvement with the increase of the Cs_2TiBr_6 layer thickness from 1.179776 V for 100 nm to 1.179815 V for 1300 nm. The PCE indicated a slight increase of the value 33.8056% for a thickness of 100 nm to the maximum value 33.8498% for a thickness of 700 nm then it decreased slightly to 33.8492% for 1300 nm. This initial increase in PCE can be explained by an increase in electron-hole pair production with the increase in Cs_2TiBr_6 thickness [29]. However, an additional increase in the Cs_2TiBr_6 layer thickness results with an increase in the strength as well as the defect density and recombination rate, explains the decrease in FF. The decrease in FF and saturated J_{sc} at thickness was greater than 700 nm results in decrease in PCE [30, 31]. The Cs_2TiBr_6 layer thickness of 700 nm produced the best results. So, it is the optimal thickness for this layer that corresponds to V_{oc} = 1.179814 V, J_{sc} = 32.33589974 mA cm^{-2}, FF = 88.7272% and PCE = 33.8498% obtained values. This thickness was used for the remaining simulations. The optimal thickness, obtained for the Cs_2TiBr_6 absorber, is slightly less than its optimal 800 nm thickness obtained in previous works [29].

For the second active layer $MASnBr_3$, the effect of $MASnBr_3$ thickness on photovoltaic parameters and $J - V$ characteristics are depicted in Fig. 3. These results display that the increase in the thickness of the $MASnBr_3$ layer had a negative effect on the V_{oc}, it decreased from 1.2042 V for a thickness of 100 nm to 1.1596 V for 1300 nm. The J_{sc} indicates a rapid increase from 19.58 to 32.34 mA cm^{-2} for thicknesses from 100 to 500 nm for thicknesses greater than 500 nm it continued to increase slowly until raising its maximum to 33.93 mA cm^{-2} for a thickness of 1100 nm then it decreased to 33.90 mA cm^{-2} for a thickness of 1300 nm. The FF increased from 87.9664 to 88.7822% for thicknesses from 100 to 700 nm and then slightly decreased to 88.7430% for 1300 nm.

The decrease in V_{oc} for thicknesses between 100 and 700 nm could be explained by the reduced mobility of charge carriers, while the improvement in charge collection could illustrate the increase in the filling factor in this region. For thicknesses greater than 700 nm both V_{oc} and FF parameters had been decreased with increasing thickness and this decrease might be due to increased charge losses and recombination phenomena, a decrease in the collection efficiency of holders [30, 32]. It is noted that the PCE values revealed an improvement with the increase of the $MASnBr_3$ layer thickness by 20.73% for 100 nm until reaching its maximum at 35.05% for 900 nm and beyond the latter, it decreased until reaching 34.89% for 1300 nm. The improvements in PCE and J_{sc} could be explained by the fact that the increase in the volume of the $MASnBr_3$ active layer would allow strong absorption of photons, which means that more carriers would be generated [30, 32]. However, a saturated J_{sc} and reduced FF, for $MASnBr_3$ thicknesses greater than 900 nm, would reduce the PCE of

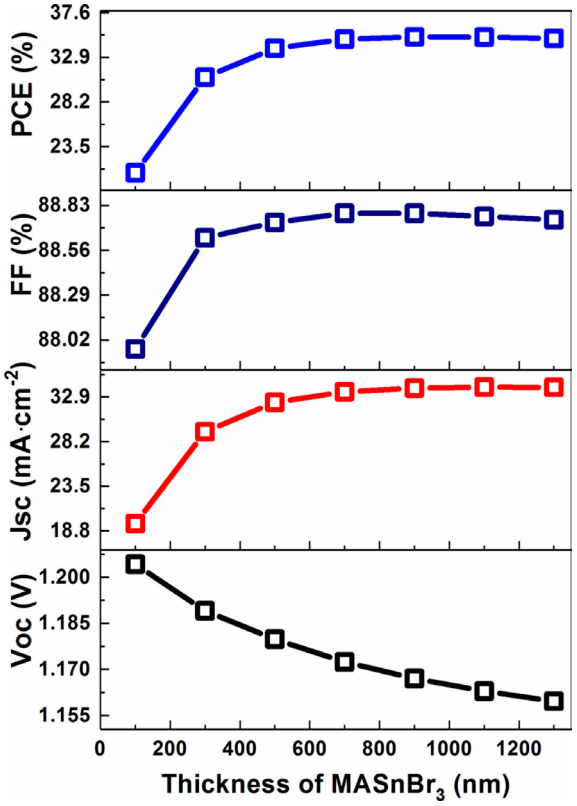

(a)

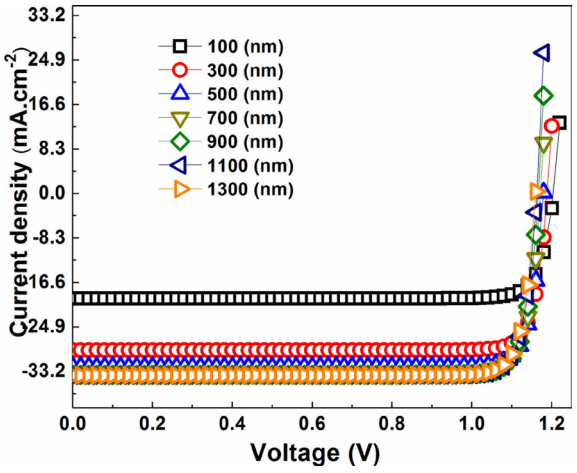

(b)

Fig. 3 (a) The effect of $MASnBr_3$ layer thickness on photovoltaic parameters of PSC device and on (b) J-V characteristics

the device $Au/MoO_3/Cs_2TiBr_6/MASnBr_3/ZnO/FTO$ [31]. The thickness of 900 nm was selected as optimal for this cell, at this value the cell produces a V_{oc} of 1.16703 V, a J_{sc} of 33.83 mA cm^{-2}, a FF of 88.78, and a PCE of 35.06%. In a simulation study carried out by Bala and Mallik, a thickness of 500 nm was chosen as optimal for $MASnBr_3$, and for this thickness the cell studied by this group produced an efficiency of about 25% [33].

3.2 Optimization of defect density in the Cs_2TiBr_6 and $MASnBr_3$ layers

Another important factor that might have a big impact on the device performance is the overall defect density of the active layer. PSCs have a variety of defects, which can be classified according to how they are generated, including atomic defects, larger defects, grain boundaries, massive defects, anti-site and interstitial substitutions [34].

Generation and recombination are crucial phenomena that occur in the absorbent layer and are caused by defects in this layer. The quality of the PSC largely depends on the quality of the absorbent layer, which will deteriorate if the defect density is large [35]. In this part, the effect of the defect density in both Cs_2TiBr_6 and $MASnBr_3$ absorbers on the cell output parameters was investigated. For this purpose the defect density has been varied from 10^{14} to 10^{20} nm, in accordance with the previous work of Mohanty et al. [35], Ouslimane et al. [36] and Sarker et al. [37].

Fig. 4 depicts the effect of defect density in the first absorbent layer Cs_2TiBr_6 on the output parameters of the cell. From these graphs, it was found that all PV parameters display a slight decrease with the increase of the

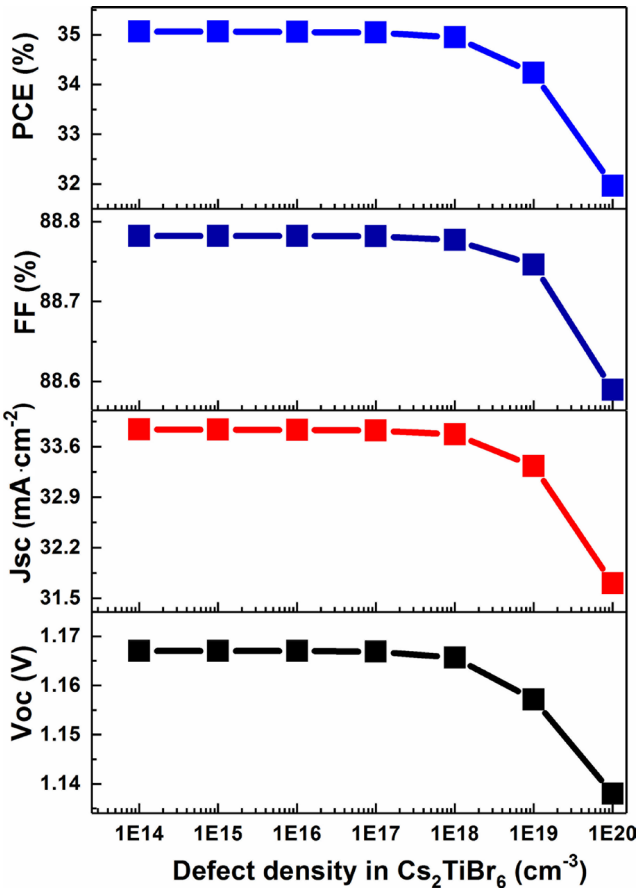

Fig. 4 The photovoltaic parameters as a function of the defect density in Cs_2TiBr_6

defect density from 10^{14} to 10^{18} cm^{-3}, while they decrease rapidly for the defect density greater than 10^{18} cm^{-3}. For defect densities from 10^{14} to 10^{18} cm^{-3} the V_{oc}, J_{sc}, FF and PCE decreased slightly from 1.1670 to 1.1656 V, 33.84 to 33.77 mA cm^{-2}, 88.782 to 88.777% and 35.06 to 34.95% respectively. These results are consistent with those reported by and Islam and Paul, which also found a decrease in all photovoltaic parameters with the increase in defect densities, attributed to an increase in recombination losses [12]. This slight decrease was probably due to the diffusion length of the charge carriers which is sufficient for them to draw through the Cs_2TiBr_6 active layer without recombining. Once the defect density exceeded 10^{18} cm^{-3} they decreased sharply until they reached their minimum respectively at 1.1379 V, 31.71 mA cm^{-2}, 88.59% and 31.97% for a defect density of 10^{20} cm^{-3}.

This sharp decrease in the output parameters of the cell is due to the reduction of the life of the charge carriers with the increase of the defect density in Cs_2TiBr_6 resulting in a significant recombination at the Cs_2TiBr_6/$MASnBr_3$ interface [25]. These results are confirmed by Fig. 5 which illustrates the effect of the defect density in Cs_2TiBr_6 on the recombination rate for both 10^{14} and 10^{20} cm^{-3}. From its curves it is clear that at the Cs_2TiBr_6/$MASnBr_3$ interface the recombination rate became important for a large defect density (10^{20} cm^{-3}). The value 10^{14} cm^{-3} was selected as the optimal value and used as the defect density in Cs_2TiBr_6 for the remaining simulations, this value corresponded to a V_{oc} of 1.1670 V, a J_{sc} of 33.84 mA cm^{-2}, a FF of 88.782% and a PCE of 35.06%.

In the same way the effect of the defect density in the second active layer $MASnBr_3$ on the PV parameters was studied. The results are depicted in Fig. 6. All cell performance degraded rapidly and sharply with the increase in defect density in $MASnBr_3$. The V_{oc}, the J_{sc}, the FF and the PCE go respectively from 1.167 V, 33.84 mA cm^{-2}, 88.78% and 35.06% for 10^{14} cm^{-3} to 0.501 V, 2.51 mA cm^{-2}, 60.43% and 0.76% for the maximum defect density 10^{20} cm^{-3}. Fig. 7 depicts the variation in recombination rates for a minimum and maximum defect density (10^{14} and 10^{20} cm^{-3}) as a function of cell thickness. According to its graphs, a maximum defect density of 10^{20} cm^{-3} had a large impact on the recombination rate at the $MASnBr_3$/ZnO interface, degradation of PV parameters might be due to the improvement in the recombination rate which is the result of the decrease in the lifetime of charge carriers with the increase in defect density in $MASnBr_3$. The best performances produced by the cell were obtained for a defect density of 10^{14} cm^{-3}, this value was selected as the optimal value of the defect density in the perovskite layer $MASnBr_3$, it corresponded to V_{oc} of 1.167 V, J_{sc} of 33.84 mA cm^{-2}, FF of 88.78% and PCE of 35.06%. Ashfaq et al. proposed a cell based on three perovskite layers, this cell produced an efficiency of 13.19%, for a defect density of 10^{12} cm^{-3} [13].

3.3 Optimization of defect density in HTM/Cs_2TiBr_6, HTM/Cs_2TiBr_6, Cs_2TiBr_6/$MASnBr_3$ and $MASnBr_3$/ETM interfaces

Interface defects have a significant impact on PSC stability, as they trap photogenerated carriers and reduce their

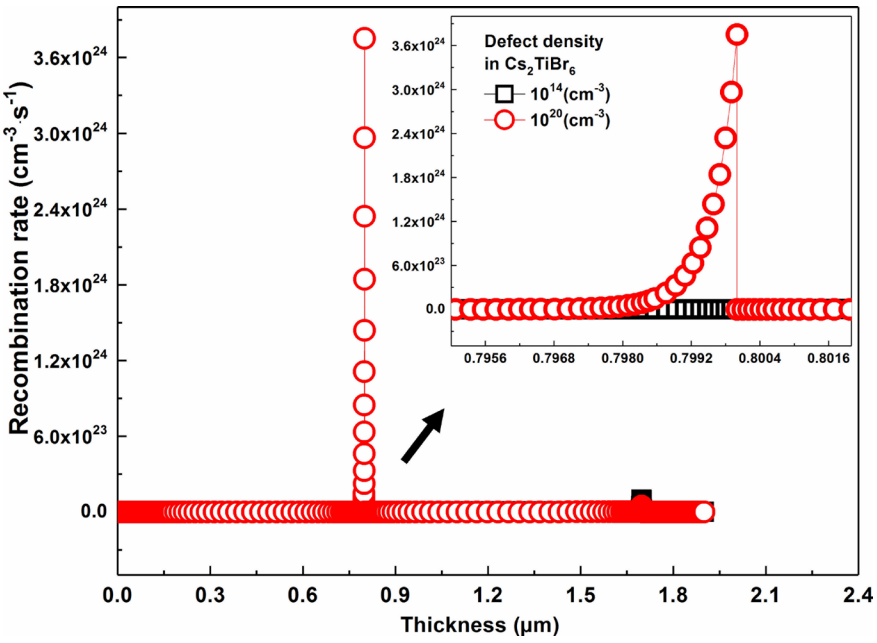

Fig. 5 The effect of defect density in Cs_2TiBr_6 on the recombination rate

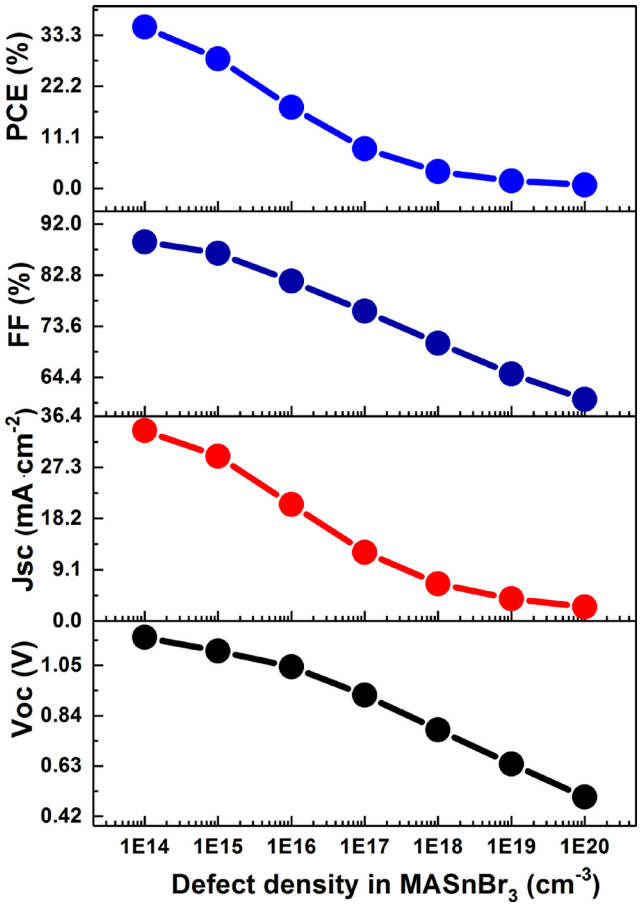

Fig. 6 The photovoltaic parameters as a function of the defect density in $MASnBr_3$

lifetime, resulting in high recombination rates. This type typically resulted from the manufacturing process of the devices, resulting in hanging bonds to grain joints and interfaces [2, 38]. In this part, the effect of the defect density in the three interfaces on PSC performance: HTM/Cs_2TiBr_6, Cs_2TiBr_6/$MASnBr_3$ and $MASnBr_3$/ETM was studied independently.

To study its impact on the cell performance proposed in this study, the defect density in the three interfaces HTM/Cs_2TiBr_6, Cs_2TiBr_6/$MASnBr_3$ and $MASnBr_3$/ETM was varied respectively from 10^{10} to 10^{20} cm^{-2}, and each time the optimal density was obtained it is used for the following simulations. The results are depicted in Figs. 8, 9 and 10 respectively. As illustrated in Fig. 8, the change in the defect density in the HTM/Cs_2TiBr_6 interface had no effect on the output parameters of the cell all PV parameters such as V_{oc}, J_{sc}, FF and PCE remained constant at 1.167 V respectively, 33.84 mA cm^{-2}, 88.78% and 35.06%. Although the best performance had been obtained for defect densities of 10^{10} and 10^{12} cm^{-2}, the low defect density material is difficult to synthesize. Therefore, the defect density of the order of 10^{14} cm^{-2} was selected as the optimal fault density for the HTM/Cs_2TiBr_6 interface, the latter corresponds to a V_{oc} of 1.167 V, a J_{sc} of 33.84 mA cm^{-2}, a FF of 88.78%, and a PCE of 35.06%. For the subsequent simulations, the defect density in the HTM/Cs_2TiBr_6 interface was set to 10^{14} cm^{-2}.

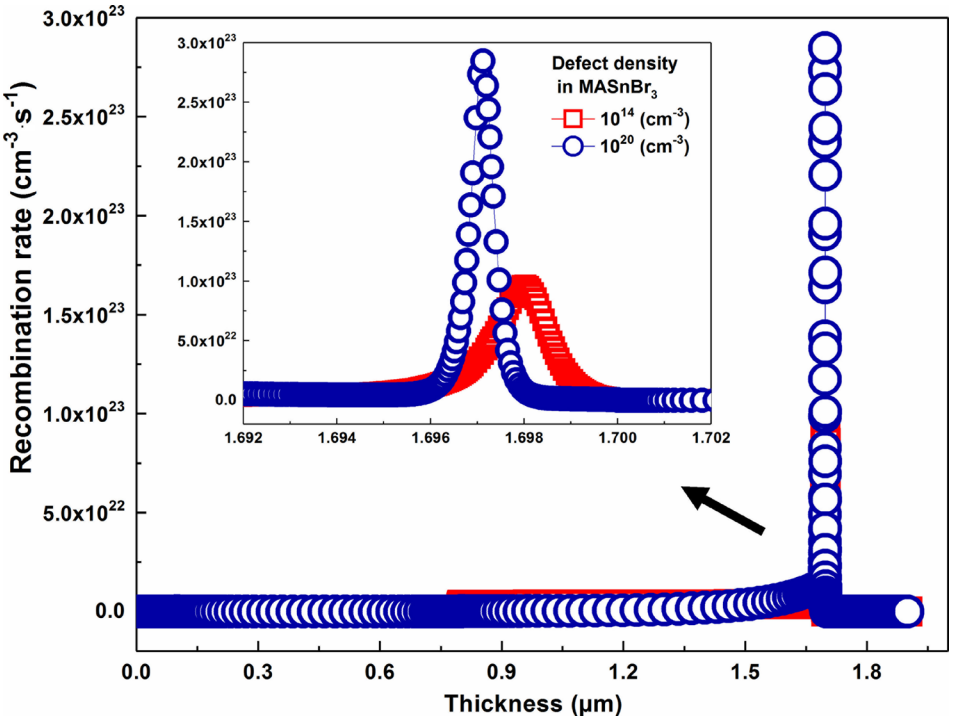

Fig. 7 The effect of defect density in $MASnBr_3$ on the recombination rate

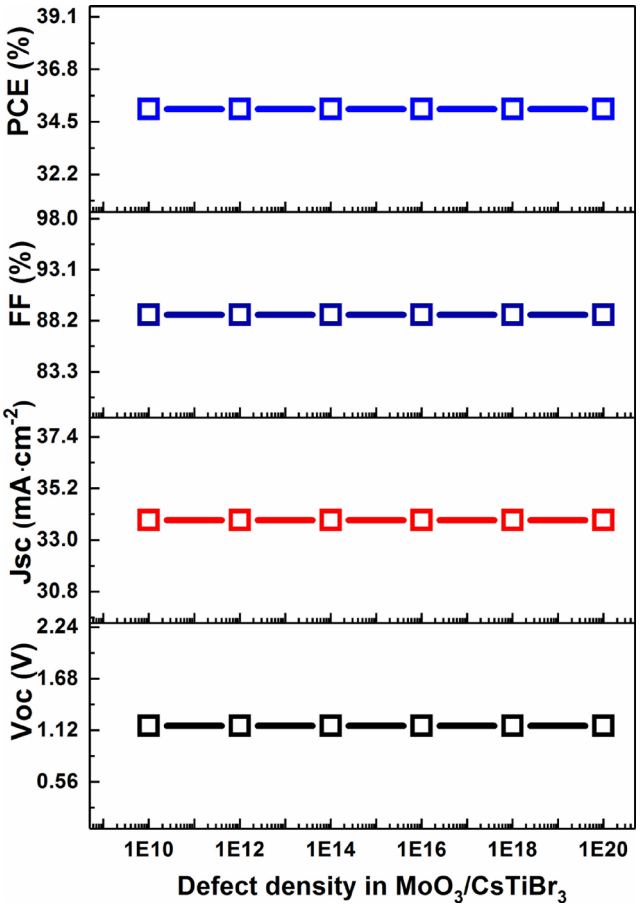

Fig. 8 The effect of the defect density in MoO_3/Cs_2TiBr_6 on the photovoltaic parameters

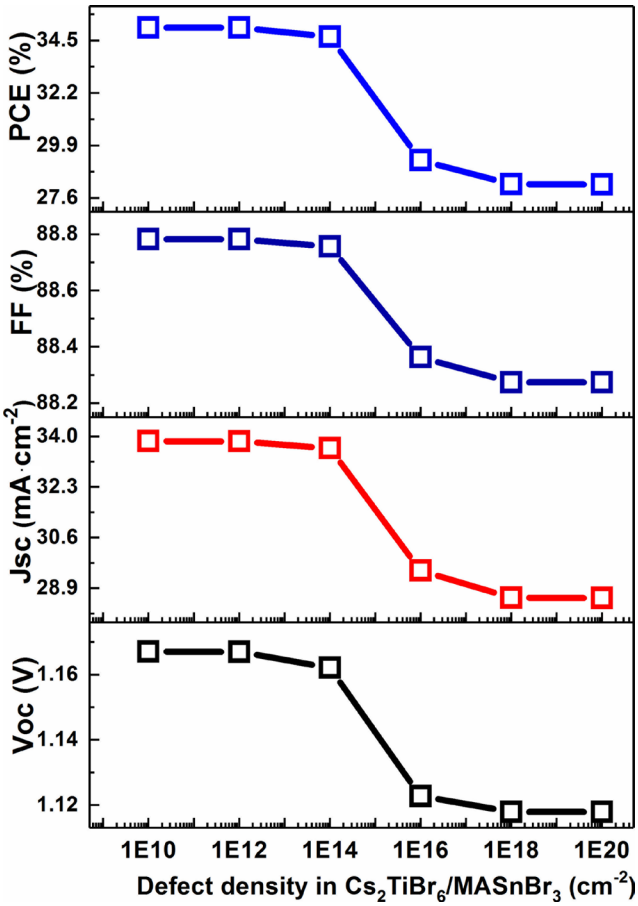

Fig. 9 The effect of the defect density in $Cs_2TiBr_6/MASnBr_3$ on the photovoltaic parameters

The variation of the defect density in the $Cs_2TiBr_6/MASnBr_3$ and $MASnBr_3$/ETM interfaces is depicted in Figs. 9 and 10 respectively. According to its graphs the effect of the defect density in those two interfaces on the PV parameters was almost similar. For defect densities below 10^{14} cm^{-2} this effect is almost negligible. Once the defect density exceeded 10^{14} cm^{-2}, all PV parameters had a sharp decrease. The value 10^{14} cm^{-2} was evaluated as optimal for the $Cs_2TiBr_6/MASnBr_3$ interface. For $Cs_2TiBr_6/MASnBr_3$ interface, the V_{oc}, J_{sc}, FF and PCE decrease slightly by 1.16 V_{oc}, 33 mA cm^{-2}, 88.8%, 35% for defect densities less than 10^{14} cm^{-2}. Beyond the value 10^{14} cm^{-2} all the parameters followed the same behavior and decreased strongly until reaching its minimum respectively at 1.117850 V, 28.56681205 mA cm^{-2}, 88.2730% and 28.1886% for 10^{20} cm^{-2}. The decrease in parameters with the increase in defect density in $Cs_2TiBr_6/MASnBr_3$ might be due to the increased possibility of recombinant charge carriers in the $MASnBr_3$ layer. The defect density of 10^{14} cm^{-2} was selected as the optimal density of the $Cs_2TiBr_6/MASnBr_3$ interface which corresponded to V_{oc} of 1.162092 V, J_{sc} of 33.60183670 mA cm^{-2}, FF of 88.7565% and PCE of 34.6580%. The defect density in $Cs_2TiBr_6/MASnBr_3$ was set to 10^{14} cm^{-2} for the remaining simulations.

Similarly, for the $MASnBr_3$/ETM interface, all PV parameters such as V_{oc}, J_{sc}, FF and PCE remained almost at 1.16 V, 33.60 mA cm^{-2}, 88.7% and 35% respectively for defect densities below 10^{14} cm^{-2}. Beyond 10^{14} cm^{-2} all PV parameters decreased to its minimum respectively at 0.937 V, 33.38 mA cm^{-2}, 86.24% and 26.98% for a defect density of 10^{20} cm^{-2}. The degradation of the I-V characteristics of the cell with the increase of the defect density in the $MASnBr_3$/ETM interface could be caused by the reduction of the collected charge carriers. In fact, the increase in defect density at the $MASnBr_3$/ETM interface reduced the transition of the charge carriers from the $MASnBr_3$ absorption layer to the ETM layer, and those carriers were actually recombined, trapped or dispersed. The value of 10^{14} cm^{-2} was taken as the optimal value of the defect density for the $MASnBr_3$/ETM interface, this density corresponded to a V_{oc} of 1.158 V, a J_{sc} of 33.60 mA cm^{-2}, a FF of 88.69% and PCE of 34.51%.

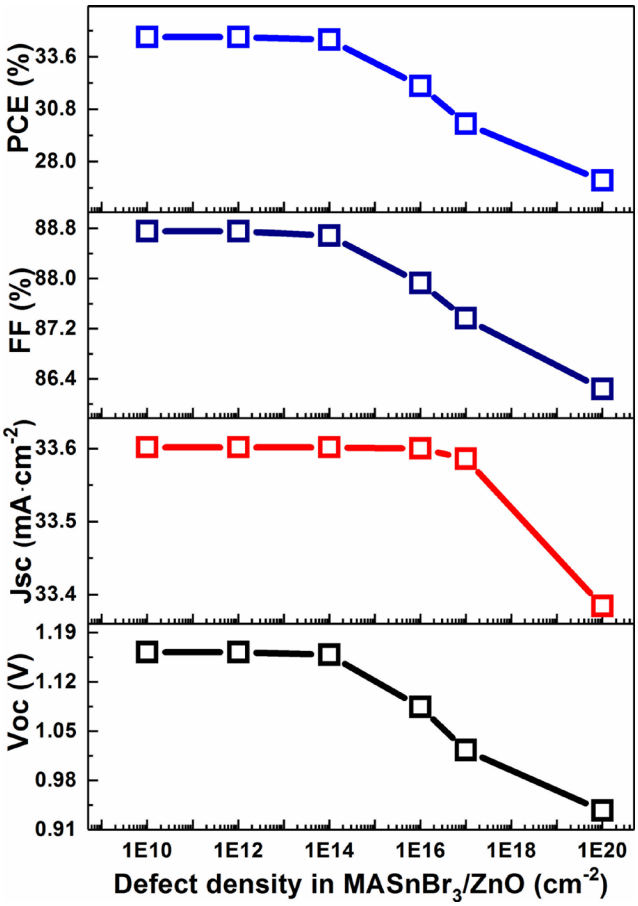

Fig. 10 The effect of the defect density in $MASnBr_3$/ZnO on the photovoltaic parameters

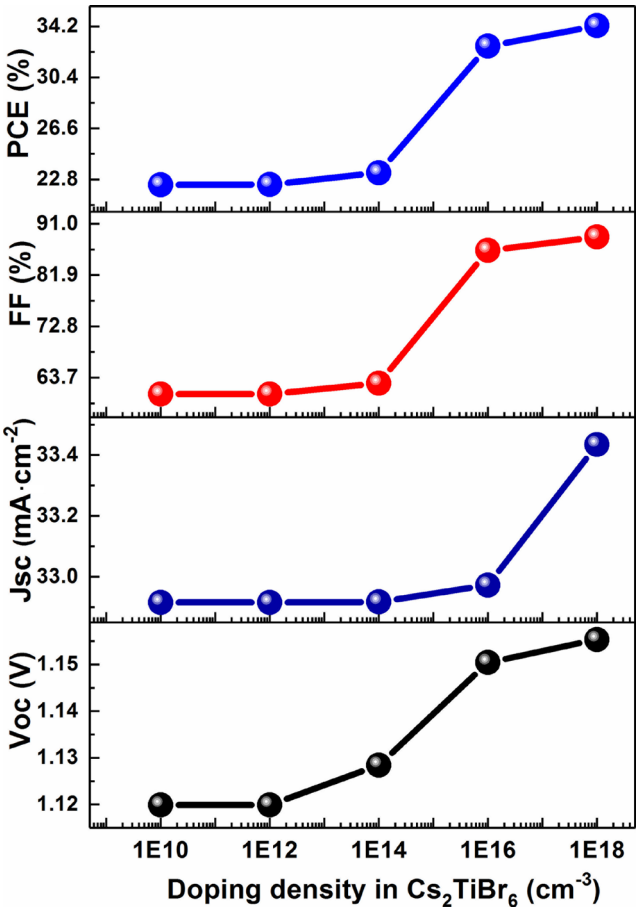

Fig. 11 The photovoltaic parameters variation as a function of doping density in Cs_2TiBr_6

3.4 Optimization of doping density in the Cs_2TiBr_6 and $MASnBr_3$ layers

The photovoltaic characteristics of the PSC was also significantly influenced by the density of the charge carriers in the absorbent layer. It is therefore a key factor in determining cell performance [25]. To study the effect of the doping density in the two Cs_2TiBr_6 and $MASnBr_3$ absorbers on the cell characteristics, the doping density was modified from 10^{10} to 10^{18} cm^{-3}. The doping effect density on PV parameters in the Cs_2TiBr_6 layer is illustrated in Fig. 11. Based on these curves, V_{oc}, J_{sc}, FF and PCE had the same behavior, they presented almost no change for doping densities less than 10^{14} cm^{-3}, and for doping densities greater than 10^{14} cm^{-3}, they increase to 1.155 V, 33.44 mA cm^{-2}, 88.67% and 34.25% respectively for a doping density of 10^{18} cm^{-3}. To understand these results the variation of electric fields was plotted as a function of the cell thickness for a doping density of 10^{10} cm^{-3} and 10^{18} cm^{-3} for the Cs_2TiBr_6 layer, the graphs obtained are depicted in Fig. 12. From these graphs, it could be seen that for a high doping density of the order of 10^{18} cm^{-3} in Cs_2TiBr_6, the electric field became important at the HTM/Cs_2TiBr_6 interface compared to the low doping density. The field improvement facilitated the separation and collection of photo-generated charge carriers, which improved the cell performance. This behavior of the $J-V$ parameters followed the same behavior of the parameters produced by the heterojunction proposed by Islam and Paul which based on Cs_2TiX_6, this optimized structure reached a PCE of 27.36% for a doping density of 10^{20} cm^{-3} for p-Cs_2TiX_6 [12]. The best performance of the (Au/MoO_3/Cs_2TiBr_6/$MASnBr_3$/ZnO/FTO) cell was obtained for a doping density of 10^{18} cm^{-3} in the Cs_2TiBr_6 layer which corresponded to 1.155 V, 33.44 mA cm^{-2}, 88.67% and 34.25%. This density was chosen as optimal for the doping density of the Cs_2TiBr_6 layer. So, the latter was used for the rest of the simulation. Fig. 13 illustrates the impact of the doping density in the $MASnBr_3$ layer on the cell output parameters. Based on these graphs, V_{oc}, J_{sc}, FF and PCE values remained constant for doping densities below 10^{14} cm^{-3} respectively at 0.993 V, 34.63 mA cm^{-2}, 80% and 27.77%. Beyond 10^{14} cm^{-3}, the J_{sc} showed a slight decrease up to 33.9 mA cm^{-2} for 10^{18} cm^{-3}, while the V_{oc}, the FF and PCE

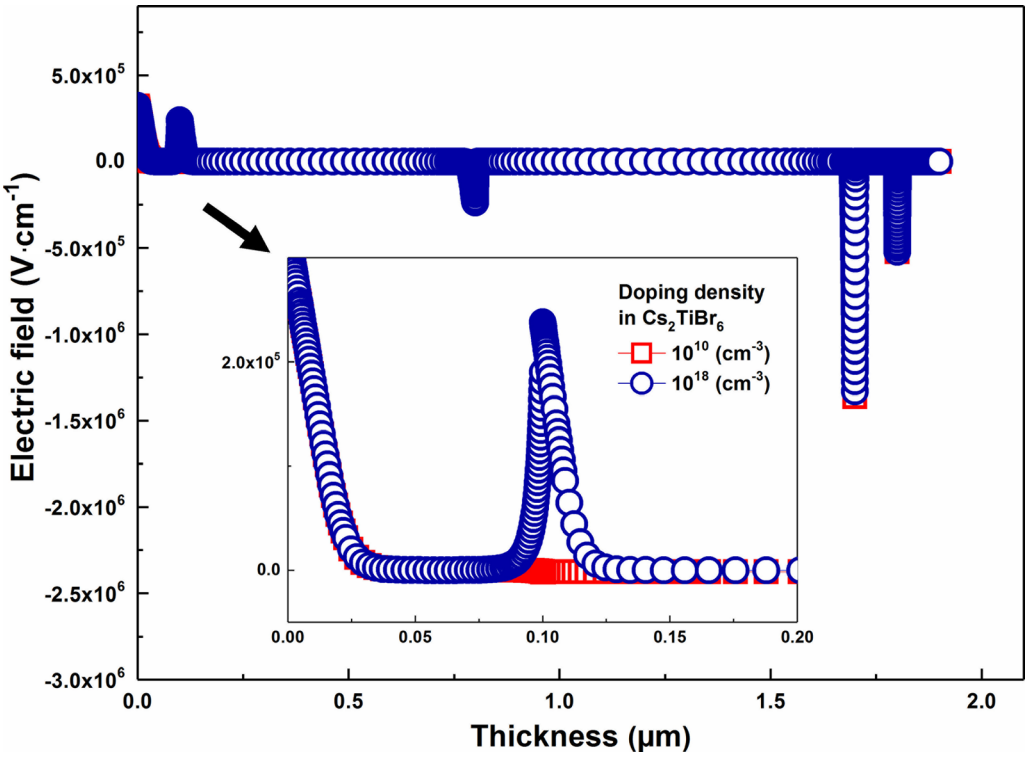

Fig. 12 The electric field profile versus thickness layer for 10^{10} and 10^{18} cm^{-3} doping density in Cs_2TiBr_6

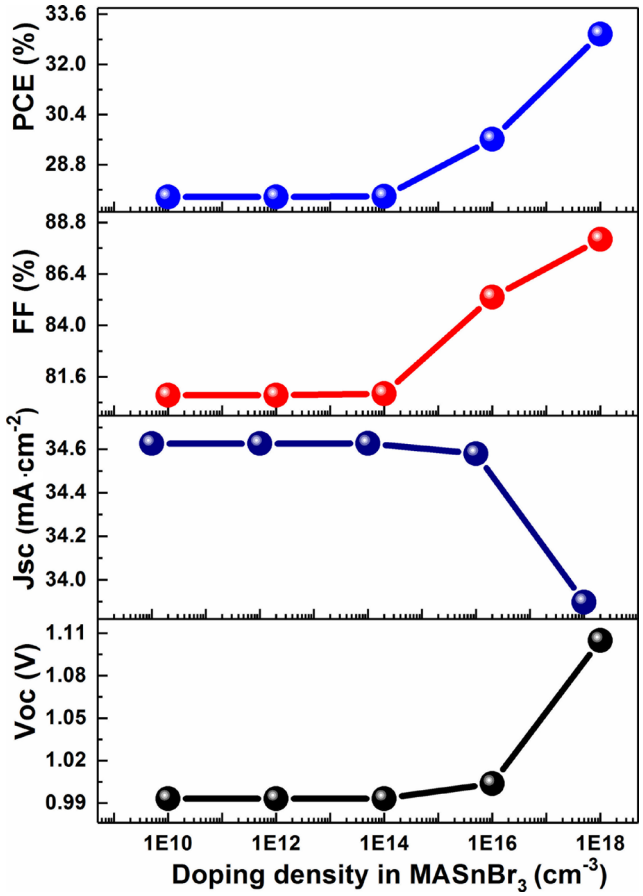

Fig. 13 The photovoltaic parameters variation as a function of doping density in $MASnBr_3$

increased with the increase of the doping density until reaching its maximums at 1.105 V, 88.01% and 32.96%. The defect density impact in the $MASnBr_3$ layer on the electric field for a low and high doping density was plotted as shown in Fig. 14. These graphs express that the doping density had a significant effect on the electric field at the $Cs_2TiBr_6/MASnBr_3$ interface. A high doping density in the $MASnBr_3$ layer generated a large electrical field at the $Cs_2TiBr_6/MASnBr_3$ interface, this important field at this level of the solar cell facilitated the separation and collection of photo-generated charge carriers. The optimal doping density for the $MASnBr_3$ layer was chosen at 10^{18} cm^{-3}, for this density the cell produces a V_{oc} of 1.105 V, a J_{sc} of 33.9 mA cm^{-2}, a FF of 88.01% and a PCE of 32.96%. This value was used for all other remaining simulations.

3.5 The influence of temperature

Temperature has a significant impact on the functioning of solar cells. In the present study, the influence of temperature was studied by adjusting the temperature between 300 and 440 K. In fact, solar panels were mounted outdoors and generally operate at temperatures above 300 K. Therefore, a high temperature caused a change in the resistance in series, which affected the charge carrier density, the mobility and the band gap of various cellular materials resulting in a degradation of the various photovoltaic

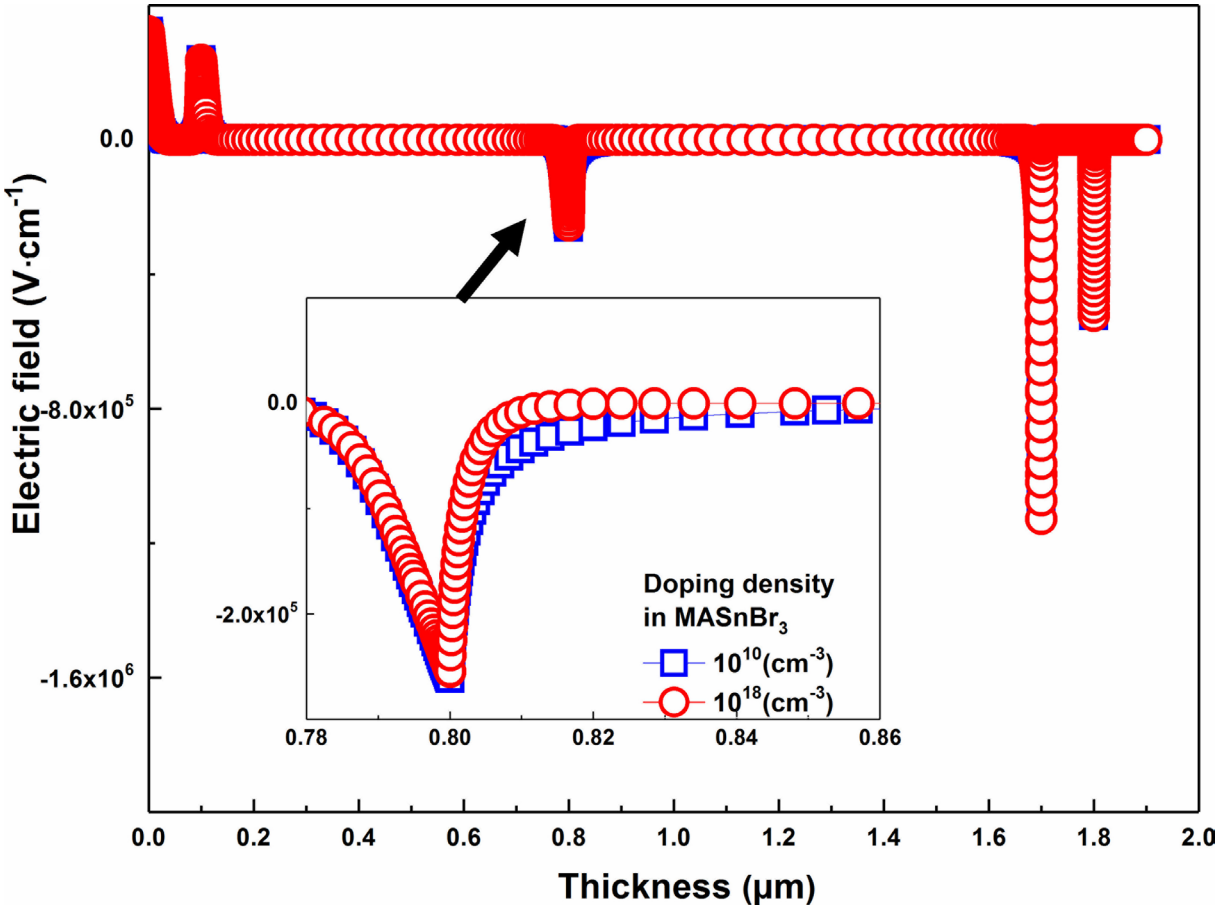

Fig. 14 The electric field profile versus thickness layer for 10^{10} and 10^{18} cm^{-3} doping density in $MASnBr_3$

properties of the cell. In addition, a high temperature increased the number of interfacial defects in the device and decreased the interconnectivity between the cell layers [4, 39]. In order to study the impact of temperature on the functioning of the proposed cell ($Au/MoO_3/Cs_2TiBr_6/MASnBr_3/ZnO/FTO$), the temperature was varied from 300 to 440 K [35]. Fig. 15 illustrates the effect of temperature variation on the PV parameters of the cell.

The curves display that the increase in temperature causes a slight improvement in the current density of short circuit from 33.90 mA cm^{-2} for 300 K to 34.07 mA cm^{-2} for 440 K. This increase in J_{sc} might be due to the reduction in bandwidth and the improvement in thermal production of carriers that increased with the increase in temperature [16]. On the other hand, the increase in temperature has a negative impact on PCE, FF and V_{oc}. PCE decreased from 32.96 to 27.02% and FF decreased from 88.01 to 82.78%, while V_{oc} decreased from 1.105 to 0.958 V, for temperatures from 300 to 440 K. This decrease in PV parameters (PCE, FF and V_{oc}) with temperature growth might be due to the decrease in diffusion length, and consequently this reduction results in an improvement in recombination rate [16, 40]. This cell is able to withstand a wide temperature range without degrading, as demonstrated by its remarkable ability to maintain a PCE greater than 27.02% in the temperature range 300–440 K. The temperature 300 K could be chosen as optimal for this cell, PV parameters corresponding to this value are V_{oc} = 1.105 V, J_{sc} = 33.90 mA cm^{-2}, FF = 88.01% and PCE 32.96%.

3.6 Effect of series R_s and shunt R_{sh} resistance

Series resistance (R_s) is one of the essential detrimental factors in the manufacture of high-performance solar cells. The majority of solar cells include R_s due to the circulation of electric current through the base and transmitter, and the contact resistance in the interfaces. The decrease in FF is the main way that R_s affects the efficiency of the solar cell. It could also affect the electrical current generation of the solar cell, as expressed in equation [37, 41]:

$$I = I_L - I_0 \exp\left(\frac{q(V + IR_s)}{nk_BT}\right), \tag{9}$$

where I_L is the current generated by solar irradiation, q is the charge of the electron, V is the voltage through the

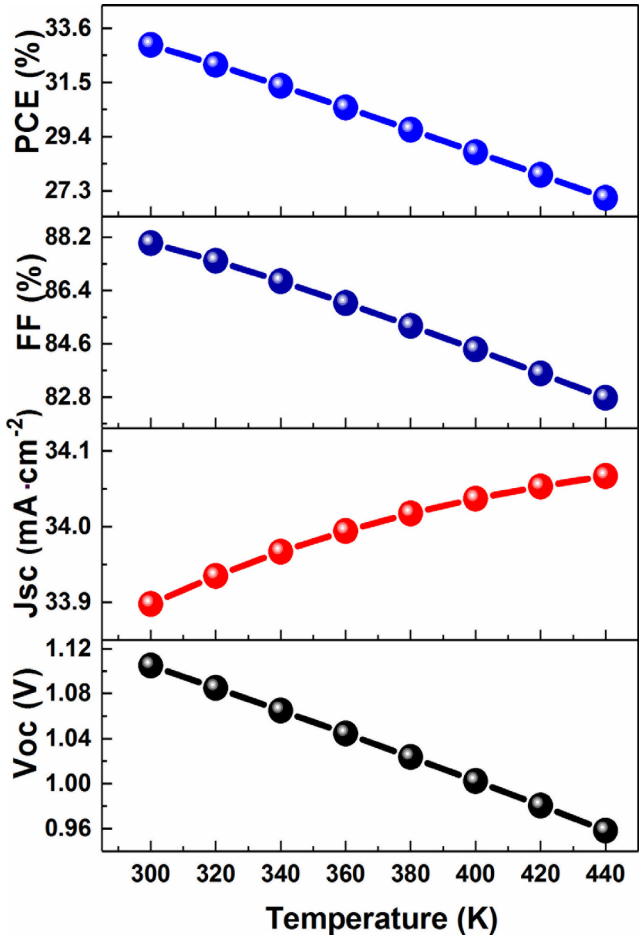

(a)

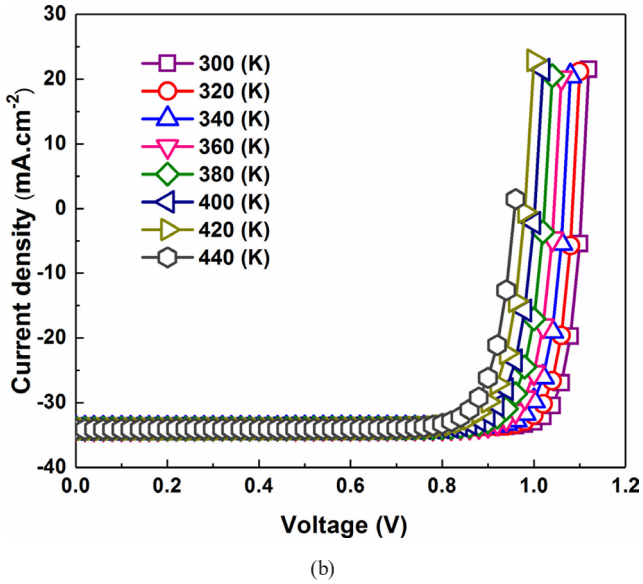

(b)

Fig. 15 (a) Influence of temperature on PV parameters and on (b) J-V characteristics

terminals of the cell, I is the output current of the cell, R_s is the resistance of the cell series, n is the ideality factor, k_B is Boltzmann constant and T is the operating temperature.

In this research, the effect of the series resistance variation on the photovoltaic parameters of the proposed cell ($Au/MoO_3/Cs_2TiBr_6/MASnBr_3/ZnO/FTO$) was studied, as depicted in Fig. 16. The resistance in series was varied from 0 to 40 Ω cm^2 at intervals of 5 Ω cm^2. The results showed that the variations of the photovoltaic parameters with the variation of R_s are consistent with the fundamental physics of the operational devices. For higher R_s, the V_{oc} exhibited a slight increase from 1.10490 to 1.10585 while J_{sc}, FF and PCE decrease respectively from 33.90 to 26.54 mA cm^{-2}, from 88.01 to 21.44% and from 32.96 to 6.29% for R_s from 0 to 40 Ω cm^2, due to the increased potential reduction. As it can be seen, the use of values above 10 Ω cm^2 provides a comparatively low PCE (below 22.45%). R_s below 5 Ω cm^2 can be considered optimal values for this cell. The suggested R_s less than 5 Ω cm^2 could be achieved by sophisticated manufacturing methods, as reported in previous work on the subject [42].

Undivided leakage currents and recombination losses were responsible for the considerable power loss caused by the presence of shunt resistors (R_{sh}) in PSC. A partial short circuit of the junction sometimes occurs in the actual solar cells due to the creation of pinholes and the extension of the

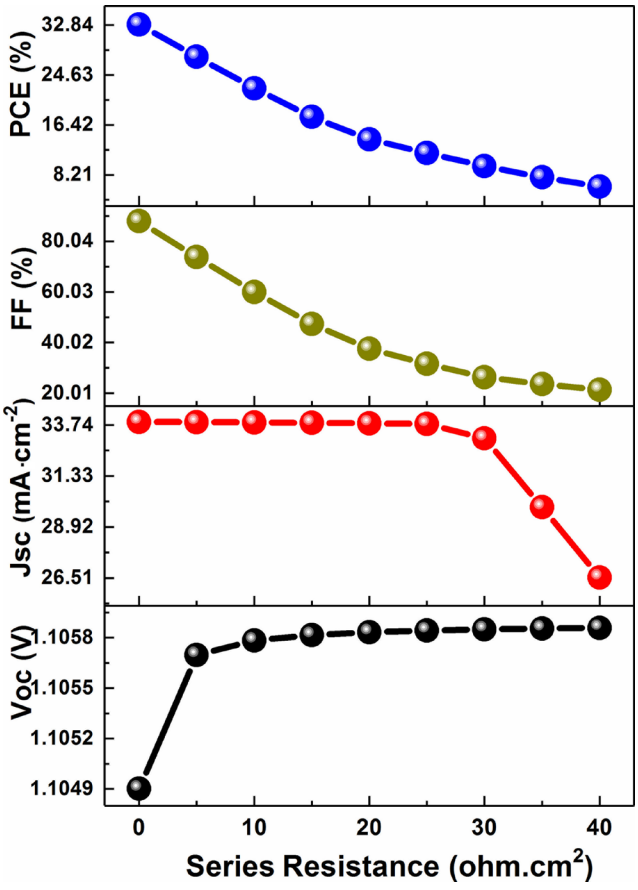

Fig. 16 The effect of the variation of R_s on PV parameters

metal filling of these pinholes in the junction. The low shunt resistance provided an alternating path for the current generated by the light, resulting in a loss of power in the solar cell. A similar deviation reduced the voltage produced by the solar cell and lowered the current passing through the SC junction. Since the photocurrent is lower in low light, the impact of the shunt resistance is more severe. Therefore, this current loss impact via the shunt is greater [43]. In addition, the shunt resistance effect is significant at lower voltages when the effective resistance of the SC is considerable.

Fig. 17 sketches the effect of shunt resistance variation from 1000 to 8000 Ω cm^2 on cell output parameters (Au/MoO_3/Cs_2TiBr_6/$MASnBr_3$/ZnO/FTO). These graphs show that the variation of R_{sh} had no effect on the J_{sc}, it remained close to the value 33.90 mA cm^{-2}, while the V_{oc}, the FF and the PCE increase with the increase of the R_{sh} respectively from 1.104 to 1.105 V, from 85.39 to 87.68% and from 31.95 to 32.84% for R_{sh} from 1000 to 8000 Ω cm^2.

The main source of R_{sh} came from defects formed during the manufacturing process. Therefore, the PCE reached a maximum value of about 32.84% at R_{sh} 8000 Ω cm^2 and this value is beneficial for obtaining a high PCE by (Au/MoO_3/Cs_2TiBr_6/$MASnBr_3$/ZnO/FTO).

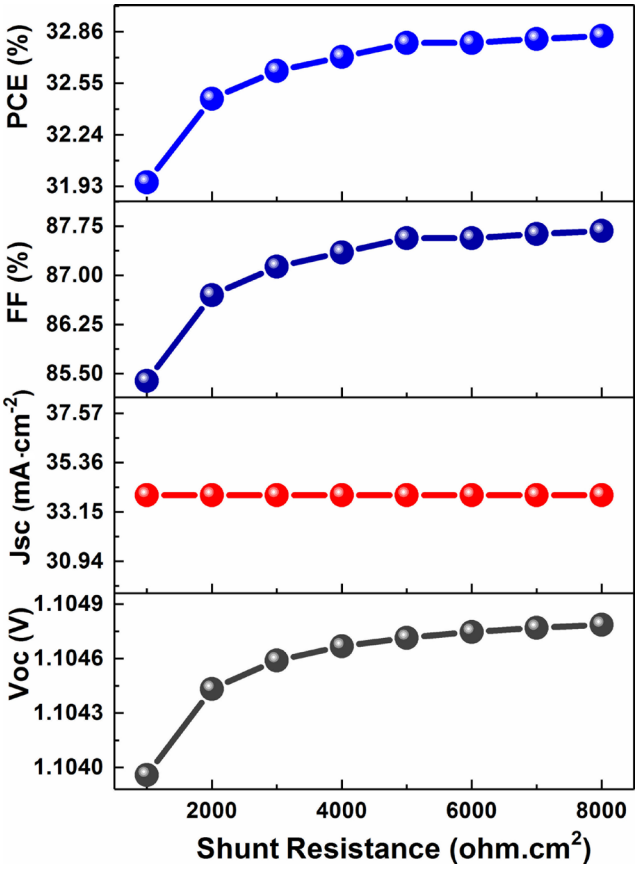

Fig. 17 The effect of the variation of R_{sh} on PV parameters

4 Conclusion

In this research, a new PSC structure with two absorber layer materials was proposed and optimized using a simulator: solar cell capacitance simulator-one dimension (SCAPS 1D). The two selected absorbers for this cell are cesium titanium bromide (Cs_2TiBr_6) and methylammonium tin bromide ($MASnBr_3$) perovskite materials. Several potential benefits of this structure have been highlighted by the results obtained and compared to traditional single layer perovskite PSCs.

The cell was composed of a molybdenum trioxide as a hole transport material, zinc oxide as electron transport material, a fluorine-doped tin oxide as a front contact and Au as a back contact, according to Au/MoO_3/Cs_2TiBr_6/$MASnBr_3$/ZnO/FTO configuration.

First, the optimization of the different parameters of this cell demonstrated that the addition of a second perovskite layer allows to significantly improve the output parameters of the cell such as a V_{oc} of 1.105 V, a J_{sc} of 33.90 mA cm^{-2}, a fill factor of 88.01% and a PCE of 32.96%. These parameters were obtained for an optimal thickness of 700 nm for Cs_2TiBr_6 and 900 nm for $MASnBr_3$, an optimal defect density of 10^{14} cm^{-3} for each layer (Cs_2TiBr_6 and $MASnBr_3$), an optimal fault density of 10^{14} cm^{-2} for each interface (HTM/Cs_2TiBr_6, Cs_2TiBr_6/$MASnBr_3$ and $MASnBr_3$/ETM) and an optimal doping density of the order of 10^{18} cm^{-3} for each absorbent layer.

In addition, the proposed PSC structure has a better tolerance to temperature changes, making it more suitable for applications in changing environments.

However, despite these promising results, further experimental studies will be needed to validate the actual performance of this new PSC structure. In conclusion, the structure of PSC proposed in this research work with two layers of perovskite materials (Cs_2TiBr_6 and $MASnBr_3$) has significant potential to improve the performance of photovoltaic devices.

Acknowledgement

The SCAPS simulation program was very helpful to the authors and was provided by Prof. M. Burgelman and his colleagues at the Department of Electronics and Information Systems at the University of Gent in Belgium. The work is included in the PRFU project under contract number B00L02UN310220220001 Oran University of sciences and technology USTO-MB.

References

[1] Kojima, A., Teshima, K., Shirai, Y., Miyasaka, T. "Organometal halide perovskites as visible-light sensitizers for photovoltaic cells", Journal of the American Chemical Society, 131(17), pp. 6050–6051, 2009.
https://doi.org/10.1021/ja809598r

[2] Pochont, N. R., Sekhar, Y. R., Vasu, K., Jose, R. "Nitrogen-Doped Titanium Dioxide as a Hole Transport Layer for High-Efficiency Formamidinium Perovskite Solar Cells", Molecules, 27(22), 7927, 2022.
https://doi.org/10.3390/molecules27227927

[3] Thakur, N., Aly, K. A., Mohery, M., Ebrahium, M. M., Kumar, P., Sharma, P. "Recent advances in $BaZrS_3$ perovskites: Synthesis, properties, and future trends", Journal of Alloys and Compounds, 957, 170457, 2023.
https://doi.org/10.1016/j.jallcom.2023.170457

[4] Mushtaq, S., Tahir, S., Ashfaq, A., Bonilla, R. S., Haneef, M., Saeed, R., Ahmad, W., Amin, N. "Performance optimization of lead-free $MASnBr_3$ based perovskite solar cells by SCAPS-1D device simulation", Solar Energy, 249, pp. 401–413, 2023.
https://doi.org/10.1016/j.solener.2022.11.050

[5] Pandey, R., Bhattarai, S., Sharma, K., Madan, J., Al-Mousoi, A. K., Mohammed, M. K. A., Hossain, M. K. "Halide Composition Engineered a Non-Toxic Perovskite-Silicon Tandem Solar Cell with 30.7% Conversion Efficiency", ACS Applied Electronic Materials, 5(10), pp. 5303–5315, 2023.
https://doi.org/10.1021/acsaelm.2c01574

[6] Ghaleb, M., Arrar, A., Touaa, Z. "Optimization and Performance Analysis of a TiO_2/i-$CH_3NH_3SnBr_3$/$CsPbI_3$/Al(BSF) Heterojunction Perovskite Solar Cell for Enhanced Efficiency", ACS Omega, 8(40), pp. 37011–37022, 2023.
https://doi.org/10.1021/acsomega.3c03891

[7] Islam, M. S., Sobayel, K., Al-Kahtani, A., Islam, M. A., Muhammad, G., Amin, N., Shahiduzzaman, M., Akhtaruzzaman, M. "Defect Study and Modelling of SnX3-Based Perovskite Solar Cells with SCAPS-1D", Nanomaterials, 11(5), 1218, 2021.
https://doi.org/10.3390/nano11051218

[8] Kour, R., Arya, S., Verma, S., Gupta, J., Bandhoria, P., Bharti, V., Datt, R., Gupta, V. "Potential Substitutes for Replacement of Lead in Perovskite Solar Cells: A Review", Global Challenges, 3(11), 1900050, 2019.
https://doi.org/10.1002/gch2.201900050

[9] Haneef, M., Tahir, S., Mahmoud, H. A., Ali, A., Ashfaq, A. "Optimizing Lead-free $MASnBr_3$ Perovskite Solar Cells for High-Efficiency and Long-Term Stability Using Graphene and Advanced Interface Layers", ACS Omega, 9(6), pp. 7053–7060, 2024.
https://doi.org/10.1021/acsomega.3c08981

[10] Ju, M.-G. Chen, M., Zhou, Y., Garces, H. F., Dai, J., Ma, L., Padture, N. P., Zeng, X. C. "Earth-Abundant Nontoxic Titanium(IV)-based Vacancy-Ordered Double Perovskite Halides with Tunable 1.0 to 1.8 eV Bandgaps for Photovoltaic Applications", ACS Energy Letters, 3(2), pp. 297–304, 2018.
https://doi.org/10.1021/acsenergylett.7b01167

[11] Chen, M., Ju, M.-G., Carl, A. D., Zong, Y., Grimm, R. L., Gu, J., Zeng, X. C., Zhou, Y., Padture, N. P. "Cesium Titanium(IV) Bromide Thin Films Based Stable Lead-free Perovskite Solar Cells", Joule, 2(3), pp. 578–570, 2018.
https://doi.org/10.1016/j.joule.2018.01.009

[12] Islam, M. A., Paul, R. "A lead-free inorganic Cs_2TiX_6-based heterostructure perovskite solar cell design and performance evaluation", Optical and Quantum Electronics, 55(11), 957, 2023.
https://doi.org/10.1007/s11082-023-05238-1

[13] Ashfaq, A., Tahir, S., Mushtaq, S., Alqurashi, R. S., Haneef, M., Almousa, N., Rehman, U. u., Bonilla. R. S. "Comparative performance analysis of Cs_2TiX_6 ($X = Br^-, Cl^-, I^-$) lead-free perovskite solar cells incorporating single, double and triple layer halides by SCAPS −1D", Materials Today Communications, 35, 106016, 2023.
https://doi.org/10.1016/j.mtcomm.2023.106016

[14] Mortadi, A., El Hafidi, E. M., Nasrellah, H., Monkade, M., El Moznine, R. "Investigation of bandgap grading on performances of perovskite solar cell using SCAPS-1D and impedance spectroscopy", Solar Energy Advances, 4, 100056, 2024.
https://doi.org/10.1016/j.seja.2024.100056

[15] Mortadi, A., El Hafidi, E., Monkade, M., El Moznine, R. "Investigating the influence of absorber layer thickness on the performance of perovskite solar cells: A combined simulation and impedance spectroscopy study", Materials Science for Energy Technologies, 7, pp. 158–165, 2024.
https://doi.org/10.1016/j.mset.2023.10.001

[16] Ahmed, S., Jannat, F., Khan, M. A. K., Alim, M. A. "Numerical development of eco-friendly Cs_2TiBr_6 based perovskite solar cell with all-inorganic charge transport materials via SCAPS-1D", Optik, 225, 165765, 2021.
https://doi.org/10.1016/j.ijleo.2020.165765

[17] Shivesh, K., Alam, I., Kushwaha, A. K., Kumar, M., Singh, S. V. "Investigating the theoretical performance of Cs_2TiBr_6-based perovskite solar cell with La-doped $BaSnO_3$ and $CuSbS_2$ as the charge transport layers", International Journal of Energy Research, 46(5), pp. 6045–6064, 2022.
https://doi.org/10.1002/er.7546

[18] Hossain, T., Hossain, M. S., Ali, M. H., Chakma, U., Kumer, A. Islam, M. J. "Investigation of Optoelectronics, Thermoelectric, Structural and Photovoltaic Properties of $CH_3NH_3SnBr_3$ Lead-Free Organic Perovskites", Chemical Methodologies, 5(3), pp. 259–270, 2021.
https://doi.org/10.22034/chemm.2021.130180

[19] Zheng, D., Wang, G., Huang, W., Wang, B., Ke, W., Logsdon, J. L., Wang, H., Wang, Z., Zhu, W., Yu, J., Wasielewski, M. R., Kanatzidis, M. G., Marks, T. J., Facchetti, A. "Combustion Synthesized Zinc Oxide Electron-Transport Layers for Efficient and Stable Perovskite Solar Cells", Advanced Functional Materials,29(16), 1900265, 2019.
https://doi.org/10.1002/adfm.201900265

[20] Bouazizi, S., Tlili, W., Bouich, A., Soucase, B. M., Omri, A. "Design and efficiency enhancement of FTO/$PC_{60}BM$/$CsSn_{0.5}Ge_{0.5}I_3$/Spiro-OMeTAD/Au perovskite solar cell utilizing SCAPS-1D Simulator", Materials Research Express, 9, 096402, 2022.
https://doi.org/10.1088/2053-1591/ac8d52

[21] Yousuf, R., Qazi, G. "Numerical modelling: Design and investigation of uniformly and non-uniformly doped absorber layer based PN homojunction perovskite solar cell variants", Solar Energy, 228, pp. 427–438, 2021.
https://doi.org/10.1016/j.solener.2021.09.079

[22] Qiao, Z., Zhang, M., Wu, B., Zhang, T., Ruan, Y., Chen, J., Huang, L., Wu, J., Qi, Y., Yang, X. "Inorganic tin-based perovskite solar cells: Modeling and performance analysis of hole transport layer-free structures", Chemical Physics Letters, 813, 140295, 2023.
https://doi.org/10.1016/j.cplett.2022.140295

[23] Ijaz, S., Raza, E., Ahmad, Z., Zubair, M., Mehmood, M. Q., Mehmood, H., Massoud, Y., Rehman, M. M. "Numerical simulation to optimize the efficiency of HTM-free perovskite solar cells by ETM engineering", Solar Energy, 250, pp. 108–118, 2023.
https://doi.org/10.1016/j.solener.2022.12.027

[24] Burgelman, M., Nollet, P., Degrave, S. "Modelling polycrystalline semiconductor solar cells", Thin Solid Films, 361–362, pp. 527–532, 2000.
https://doi.org/10.1016/S0040-6090(99)00825-1

[25] Saikia, D., Bera, J., Betal, A., Sahu, S. "Performance evaluation of an all inorganic $CsGeI_3$ based perovskite solar cell by numerical simulation", Optical Materials, 123, 111839, 2022.
https://doi.org/10.1016/j.optmat.2021.111839

[26] Gan, Y., Bi, X., Liu, Y., Qin, B., Li, Q., Jiang, Q., Mo, P. "Numerical Investigation Energy Conversion Performance of Tin-Based Perovskite Solar Cells Using Cell Capacitance Simulator", Energies, 13(22), 5907, 2020.
https://doi.org/10.3390/en13225907

[27] Hossain, M. K., Rubel, M. H. K., Toki, G. F. I., Alam, I., Rahman, M. F., Bencherif, H. "Effect of Various Electron and Hole Transport Layers on the Performance of $CsPbI_3$-Based Perovskite Solar Cells: A Numerical Investigation in DFT, SCAPS-1D, and wxAMPS Frameworks", ACS Omega, 7(47), pp. 43210–43230, 2022.
https://doi.org/10.1021/acsomega.2c05912

[28] Puente-López, E., Pal, M. "Numerical simulation and optimization of physical properties for high efficiency $CuSbS_2$ thin film solar cells", Optik, 272, 170233, 2023.
https://doi.org/10.1016/j.ijleo.2022.170233

[29] Jani, M. R., Islam, M. T., Al Amin, S. M., Us Sami, M. S., Shorowordi, K. M., Hossain, M. I., Chowdhury, S., Nishat, S. S., Ahmed, S. "Exploring solar cell performance of inorganic Cs_2TiBr_6 halide double perovskite: A numerical study", Superlattices and Microstructures, 146, 106652, 2020.
https://doi.org/10.1016/j.spmi.2020.106652

[30] Singh, A. K., Srivastava, S., Mahapatra, A., Baral, J. K., Pradhan, B. "Performance optimization of lead free-$MASnI_3$ based solar cell with 27% efficiency by numerical simulation", Optical Materials, 117, 111193, 2021.
https://doi.org/10.1016/j.optmat.2021.111193

[31] Bhattarai, S., Pandey, R., Madan, J., Tayeng, S., Kalita, P. K., Ansari, M. Z, Farhat, L. B., Amami, M., Hossain, M. K. "Comparative study of distinct halide composites for highly efficient perovskite solar cells using a SCAPS-1D simulator", RSC Advances,13(38), pp. 26851–26860, 2023.
https://doi.org/10.1039/D3RA04134D

[32] Bhattarai, S., Pandey, R., Madan, J., Ahmed, F., Shabnam, S. "Performance improvement approach of all inorganic perovskite solar cell with numerical simulation", Materials Today Communications, 33, 104364, 2022.
https://doi.org/10.1016/j.mtcomm.2022.104364

[33] Bala, N., Mallik, S. K. "Comparative Study of Lead-free Perovskite Materials $MASnI_3$, $MASnBr_3$ and $MAGeI_3$ to Design, Simulate and Optimize Lead Free PSC", 62(4), pp. 292–303, 2024.
https://doi.org/10.56042/ijpap.v62i4.7435

[34] Dris, K., Benhalilibа, M. "Novel Inorganic – Organic Heterojunction Solar Cell-Based Perovskite Using Two Absorbent Materials", Nano, 18(11), 2350091, 2023.
https://doi.org/10.1142/S1793292023500911

[35] Mohanty, I., Mangal, S., Singh, U. P. "Performance optimization of lead free-$MASnI_3$/CIGS heterojunction solar cell with 28.7% efficiency: A numerical approach", Optical Materials, 122, 111812, 2021.
https://doi.org/10.1016/j.optmat.2021.111812

[36] Ouslimane, T., Et-taya, L., Elmaimouni, L., Benami, A. "Impact of absorber layer thickness, defect density , and operating temperature on the performance of $MAPbI_3$ solar cells based on ZnO electron transporting material", Heliyon, 7(3), e06379, 2021.
https://doi.org/10.1016/j.heliyon.2021.e06379

[37] Sarker, S., Islam, M. T., Raufa, A., Al Jame, H., Ahsan, S., Islam, M. S., Jani, M. R., Nishat, S. S., Shorowordi, K. M., Ahmed, S. "A simulation based incremental study of stable perovskite-on-perovskite tandem solar device utilizing non-toxic tin and germanium perovskite", Materials Today Communications, 32, 103881, 2022.
https://doi.org/10.1016/j.mtcomm.2022.103881

[38] Thakur, A., Singh, D., Gill, K.S. "Numerical simulations of 26.11% efficient planar $CH_3NH_3PbI_3$ perovskite *n-i-p* solar cell", Materials Today: Proceedings, 71, pp. 195–201, 2022.
https://doi.org/10.1016/j.matpr.2022.08.423

[39] Fan, P., Gu, D., Liang, G.-X., Luo, J.-T., Chen, J.-L., Zheng, Z.-H., Zhang, D.-P. "High-performance perovskite $CH_3NH_3PbI_3$ thin films for solar cells prepared by single-source physical vapour deposition", Scientific Reports, 6(1), 29910, 2016.
https://doi.org/10.1038/srep29910

[40] Jayan, K. D., Sebastian, V. "Comprehensive device modelling and performance analysis of $MASnI_3$ based perovskite solar cells with diverse ETM, HTM and back metal contacts", Solar Energy, 217, pp. 40–48, 2021.
https://doi.org/10.1016/j.solener.2021.01.058

[41] Karthick, S., Velumani, S., Bouclé, J. "Experimental and SCAPS simulated formamidinium perovskite solar cells: A comparison of device performance", Solar Energy, 205, pp. 349–357, 2020.
https://doi.org/10.1016/j.solener.2020.05.041

[42] Basak, A., Singh, U. P. "Numerical modelling and analysis of earth abundant Sb_2S_3 and Sb_2Se_3 based solar cells using SCAPS-1D", Solar Energy Materials and Solar Cells, 230, 111184, 2021.
https://doi.org/10.1016/j.solmat.2021.111184

[43] Hossain, M. K., Toki, G. F. I., Kuddus, A., Rubel, M. H. K., Hossain, M. M., Bencherif, H., Rahman, M. F., Islam, M. R., Mushtaq, M. "An extensive study on multiple ETL and HTL layers to design and simulation of high-performance lead-free $CsSnCl_3$-based perovskite solar cells", Scientific Reports, 13(1), 2521, 2023.
https://doi.org/10.1038/s41598-023-28506-2